DRAFT VERSION MARCH 16, 2012
Preprint typeset using LaTeX style emulateapj v. 8/13/10

arXiv:1202.1096v2 [astro-ph.HE] 15 Mar 2012

RADIO-TO-TEV PHASE-RESOLVED EMISSION FROM THE CRAB PULSAR: THE ANNULAR GAP MODEL

Y. J. DU[1], G. J. QIAO[2] AND W. WANG[1]

Draft version March 16, 2012

ABSTRACT

The Crab pulsar is a quite young famous pulsar which radiates multi-wavelength pulsed photons. The latest detection of GeV and TeV pulsed emission with unprecedented signal-to-noise ratio, supplied by the powerful telescopes: *Fermi*, MAGIC and VERITAS, challenges the current popular pulsar models, which can be a valuable discriminator to justify the pulsar high-energy-emission models.

Our work is divided into two steps. First of all, taking reasonable parameters (the magnetic inclination angle $\alpha = 45^\circ$ and the view angle $\zeta = 63^\circ$), we use the latest high-energy data to calculate radio, X-ray, γ-ray and TeV light curves from a geometric view to obtain some crucial information on emission locations. Secondly, we calculate the phase-averaged spectrum and phase-resolved spectra for the Crab pulsar and take a theoretical justification from a physical view for the emission properies as found in the first step. It is found that a Gaussian emissivity distribution with the peak emission near the null charge surface in the so-called annular gap region gives the best modeled light curves. The pulsed emission of radio, X-ray, γ-ray and TeV are mainly generated from the emission of primary particles or secondary particles with different emission mechanisms in the nearly similar region of the annular gap located in the only one magnetic pole, which leads to the nearly "phase-aligned" multi-wavelength light curves. The emission of peak 1 (P1) and peak 2 (P2) is originated from the annular gap region near the null charge surface, while the emission of bridge is mainly originated from the core gap region.

The charged particles cannot corotate with the pulsar and escape from the magnetosphere, which determines the original flowing primary particles. The acceleration electric field and potential in the annular gap and core gap are huge enough in the several tens of neutron star radii. Thus the primary particles are accelerated to ultra-relativistic energies, and produce numerous secondary particles (pairs) in the inner region of the annular gap and core gap. We emphasize that there are mainly two types of pairs, i.e., one is curvature-radiation induced (CR-induced), and the other is inverse-Compton-scattering induced (ICS-induced). The phase-averaged spectrum and phase-resolved spectra from soft X-ray to TeV band are produced by four components: synchrotron radiation from CR-induced and ICS-induced pairs dominates the X-ray band to soft γ-ray band (100 eV to 10 MeV); curvature radiation and synchrotron radiation from the primary particles mainly contribute to γ-ray band (10 MeV to ~ 20 GeV); ICS from the pairs significantly contributes to the TeV γ-ray band (~ 20 GeV to 400 GeV).

The multi-wavelength pulsed emission from the Crab pulsar can be well modeled with the annular gap and core gap model. To distinguish our single magnetic pole model from two-pole models, the convincing values of the magnetic inclination angle and the viewing angle will play a key role.

Subject headings: gamma rays: stars – pulsars: general – pulsars: individual (Crab: PSR B0531+21) – radiation mechanisms: non-thermal – X-rays: individual (PSR B0531+21) – acceleration of particles

1. INTRODUCTION

The Crab pulsar (PSR B0531+21 or PSR J0534+2200) is the second most energetic pulsar to date with a spin-down luminosity $\dot{E}_{\rm rot} = 4.6 \times 10^{38}\,{\rm erg\,s^{-1}}$. It is at a distance of $d \sim 2$ kpc, and located in the Crab Nebulae which is a center-filled remnant of a supernova discovered by the Chinese "astronomers" in 1054 AD. The Crab pulsar, a very young pulsar with a characteristic age $\tau = 1240$ yr and a characteristic magnetic field of $B_0 = 3.715 \times 10^{12}$ G, has a spin period of $P = 33$ ms (Manchester et al. 2005).

The Crab pulsar radiates multi-wavelength pulsed emission from radio (10^{-6} eV) to γ-ray (up to TeV) band, especially the new γ-ray results of the sensitive Large Area Telescope (LAT) on board the *Fermi Gamma-ray Space Telescope* (*Fermi*) and a discovery of TeV pulsed emission by the powerful VERITAS array of atmospheric Cherenkov telescopes. *Fermi* LAT presented the high-quality γ-ray (100 MeV to 20 GeV) light curves and spectral data using 8 months of survey data, and predicted an exponential power-law spectra with cut-off energies of a few GeV (Abdo et al. 2010). To verify the exponential power-law cut-off spectra, the $25 - 100$ GeV pulsed emission from the Crab pulsar has been precisely measured by MAGIC telescope (Aleksić et al. 2011). It is shown that the observed cut-off spectrum has a large deviation from the inferred exponential one. VERITAS Collaboration et al. (2011) reported that the pulsed emission above 100 GeV from the Crab pulsar has been detected by the VERITAS, and showed their light curves and spectral data with excellent signal-to-noise ratio. They declared that current popular pulsar models (e.g. outer gap and slot gap models) cannot explain the detection, and the observation might not be explained by the curvature radiation as the origin of the observed emission above 100 GeV. These findings enable us to obtain considerable insights of the magnetosphere physics, e.g., accelera-

---

[1] National Astronomical Observatories, Chinese Academy of Sciences, Jia 20 Datun Road, Beijing 100012, China; dyj@nao.cas.cn
[2] School of Physics, Peking University, Beijing 100871, China

tion electric field, emission region and the relevant emission mechanisms. The multi-wavelength phase-averaged spectrum and phase-resolved spectra can discriminate the various pulsar non-thermal emission models.

There are four major physical or geometrical magnetospheric models which have previously been proposed to explain pulsed γ-ray emission of pulsars: the polar cap model (Daugherty & Harding 1994, 1996), the outer gap model (Cheng et al. 1986a,b; Romani & Yadigaroglu 1995; Zhang & Cheng 1997; Cheng et al. 2000; Zhang et al. 2004, 2007; Hirotani 2008; Tang et al. 2008; Lin & Zhang 2009), the two-pole caustic (TPC) model or the slot gap model (Dyks & Rudak 2003; Muslimov & Harding 2003, 2004; Harding et al. 2008), and the annular gap model (Qiao et al. 2004a,b, 2007; Du et al. 2010, 2011). The distinguishing features of these pulsar models are different acceleration electric field region for primary particles and relevant emission mechanisms to radiate high energy photons (Du et al. 2011). One of the key discrepancy of the mentioned emission models is the two important geometry parameters: the magnetic inclination angle α and the view angle ζ.

Cheng et al. (2000) used a 3D single-pole outer gap model to present incipient results of light curves, phase-averaged spectrum and phase-resolved spectra for the Crab pulsar. Eight years later, Tang et al. (2008) improved the outer gap model and used a modified outer gap model considering the emission from both poles to calculate light curves, phase-averaged spectrum and phase-resolved spectra from 100 eV to 10 GeV. In the case of the larger viewing angle $\zeta = 78°$ or $\zeta = 83°$ and intermediate inclination angle $\alpha = 45°$, Zhang & Li (2009); Li & Zhang (2010) improved the 3D two-pole outer gap model (Tang et al. 2008) to present their best results of light curves, phase-averaged spectrum and GeV phase-resolved spectra. They also used physical emissivities to calculate the light curves, showed the best-fit phase-averaged spectrum using emission components from the both magnetic poles, and indicated that ICS from pairs mainly contributed to the $10^4 - 10^6$ keV band. Harding et al. (2008) used a 3D slot gap model developed from the TPC model to calculate optical-to-γ-ray light curves, phase-averaged spectrum and phase-resolved spectra for the Crab pulsar with assuming a broken power-law pair energy spectrum. Hirotani (2008) demonstrated that the slot gap model reproduces at most 20% of the observed GeV fluxes owing to the small trans-field thickness.

To well study pulsed emission from pulsars, there may be two methods: (1) one can use a physical model with a realistic accelerating electric field to directly calculate the light curves and spectra; (2) one can also utilize a reasonable assumption of numerical emissivity to calculate light curves from a geometric point of view; then obtain some valuable information of radiation locations, finally calculate the spectra and take a consistent theoretical justification from a physical point of view. In conventional cases, some scientists chose the first method. Here we choose the second way to study pulsed emission from the Crab pulsar. In this paper, we study multi-wavelength light curves, phase-averaged spectrum and phase-resolved spectra of the Crab pulsar in the annular gap model. In § 2, we briefly introduce the annular gap and core gap, pair production and calculate the acceleration potential in the annular gap. In § 3, we model the multi-wavelength light curves using the annular gap model together with a core gap. The radio emission region is identified and the reason for phase-aligned peaks of multi-wavelength light curves is explained. To model spectra of the Crab pulsar, we also calculate the multi-wavelength phase-averaged and phase-resolved spectra of radiation from both primary particles and pairs. Finally, conclusions and discussions are presented in § 4.

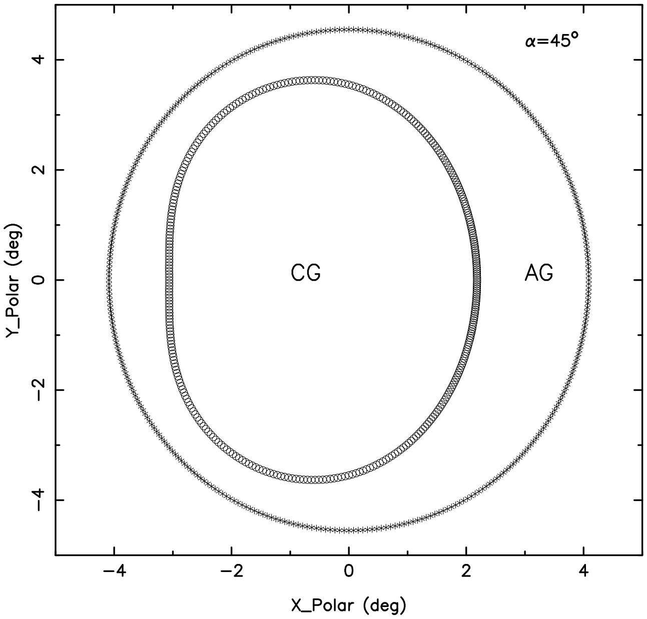

FIG. 1.— The shapes of the annular gap (AG) and core gap (CG) in the polar cap region for the crab pulsar with an inclination angle of $\alpha = 45°$. The core gap region is defined by the footpoints of critical field lines on the polar cap, and the annular gap region is between the footpoints of critical field lines and last open field lines. The annular region becomes more symmetric if α is smaller.

2. THE ANNULAR GAP AND CORE GAP

2.1. *Formation of the Annular Gap and the Core Gap*

As noted by Du et al. (2011), the open-field-line region of a pulsar magnetosphere is divided into two isolated parts by the critical field lines which denote a set of special field lines that satisfy the condition of $\mathbf{\Omega} \cdot \mathbf{B} = 0$ at the light cylinder. The core region around the magnetic axis is defined by the critical field lines, and the annular region is located between the critical field lines and the last open field lines (see Figure 1). The width of the annular polar region is anti-correlated with the pulsar period, it is therefore larger for pulsars with smaller spin periods. The annular acceleration potential is negligible for older long-period pulsars, but very important for pulsars with a small period, e.g., millisecond pulsars and young pulsars. The acceleration electric field extends from the pulsar surface to the null charge surface or even beyond it. The annular gap has a sufficient thickness of trans-field lines and a wide altitude range for particle acceleration. In the annular gap model, the high energy emission is generated in the vicinity of the null charge surface (Du et al. 2010). This leads to a wide γ-ray emission beam (Qiao et al. 2007). The radiation components from both the core gap and the annular gap can be observed simultaneously by one observer (Qiao et al. 2004b) if the inclination angle and the viewing angle are suitable.

2.2. *Acceleration Potential in the Annular Gap*

Here we will explore the formation mechanism of the acceleration electric field in the annular gap. To give a simplified picture for the powerful acceleration electric field along an open field line, we attempt to derive 1D continuous solution for the acceleration potential. Then we use this realistic

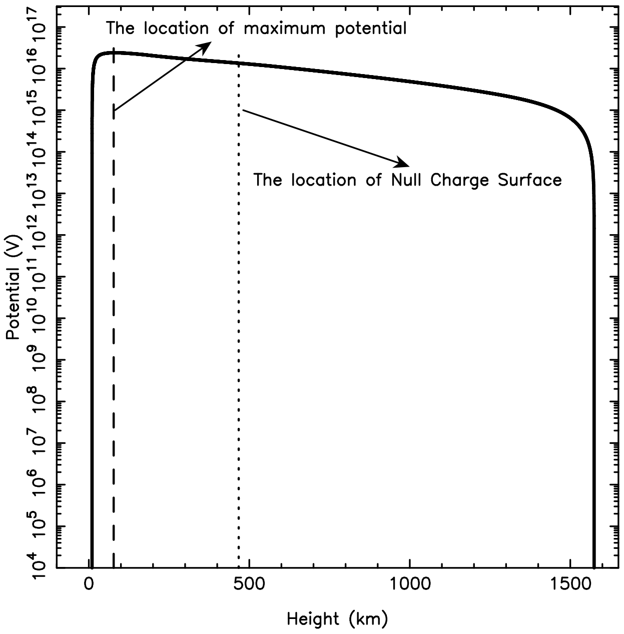

FIG. 2.— Acceleration potential on an open field line with a magnetic azimuthal $\Psi = 0^\circ$ in the annular gap. The locations of maximum potential and null charge surface are marked. The maximum potential drop on this field line is comparable to the one generated by the unipolar effect.

acceleration field to obtain the Lorentz factor $\gamma_{\rm p}$ of the primary particle which is from the balance of the acceleration and curvature radiation reaction (see Equation (5) in §2.3). The $\gamma_{\rm p}$ is not a true maximum Lorentz factor but a valuable criterion, it can be regarded as an upper limit of the real maximum Lorentz factor of the primary particles which shape the obsered spectra.

Under the assumption of a fully charge-separated magnetosphere, the outer gap can be formed (Cheng et al. 1986a). However, if abundant pairs are produced, this lead to a large neutral charge component in the magnetosphere. In this case, the acceleration mechanism of particles becomes different from the case of outer gap model.

The pulsar magnetosphere is filled with charge-separated pair plasma, and the charged particles can not co-rotate with the neutron star near the light cylinder and must escape from the magnetosphere. This is the generation mechanism for acceleration electric field. The annular gap and the core gap simultaneously export charged particles with opposite sign, which can lead to the circuit closure in the whole magnetosphere. The parallel acceleration electric field ($E_{\|}$) in the annular gap and core gap regions are opposite. As a result, $E_{\|}$ vanishes at the boundary (the critical field lines) between the annular and the core regions and also vanishes along the closed field lines. The positive and the negative charges are accelerated from the core and the annular regions, respectively.

To unveil the acceleration potential in the annular gap region, we now consider a tiny magnetic tube embedded in an open field line. We assume that the particles flow out of the co-rotating magnetosphere at a radial distance about $r_{\rm out} \sim R_{\rm LC} = 1.57 \times 10^3$ km, and that the charge density of flowing-out particles $\rho_{\rm b}(r_{\rm out})$ is equal to the local Goldreich-Julian (GJ) charge density $\rho_{\rm gj}(r_{\rm out})$ (Goldreich & Julian 1969). For any altitudes $r < r_{\rm out}$, $\rho_{\rm b}(r) < \rho_{\rm gj}(r)$. The acceleration electric field therefore exists along the field line, and cannot vanish until approaching the altitude of $r_{\rm out}$.

In a static dipole magnetic field configuration, the field components can be described as $\mathbf{B}_r = \frac{2\mu\cos\theta}{r^3}\mathbf{n}_r$ and $\mathbf{B}_\theta = \frac{\mu\sin\theta}{r^3}\mathbf{n}_\theta$, here θ is the zenith angle in magnetic coordinate, and B_0 is the surface magnetic field. Thus the magnetic field strength at a altitude r is $B(r) = \frac{B_0R^3}{2}\frac{\sqrt{3\cos^2\theta+1}}{r^3}$.

In the co-rotating frame, the equation for acceleration potential Ψ is

$$\nabla^2\Psi = -4\pi(\rho_{\rm b} - \rho_{\rm gj}). \tag{1}$$

Although the same Possion equation for acceleration field is used by all of pulsar emission models (some models also considered the relativistic effect), the key discrepancy among these models is how to obtain and explain the difference between flowing charge density and the local GJ density ($\rho_{\rm b} - \rho_{\rm gj}$). Normally it is assumed that $\rho_{\rm b} - \rho_{\rm gj} \sim 0$ at the star surface. This leads to the quite different results of the acceleration electric field.

Using the conservation laws of the particle number and magnetic flux in the magnetic flux tube, the difference between the flowing charge density and local GJ charge density at the altitude r can be written as

$$\rho_{\rm b}(r) - \rho_{\rm gj}(r) = -\frac{\Omega B(r)}{2\pi c}(\cos\zeta_{\rm out} - \cos\zeta), \tag{2}$$

where $\Omega = 2\pi/P$ is the angular velocity, P is the rotation period, and ζ and $\zeta_{\rm out}$ are the angle between the rotational axis and the B field direction at r and $r_{\rm out}$, respectively. Wang et al. (2006) found

$$\cos\zeta = \cos\alpha\cos\theta_\mu - \sin\alpha\sin\theta_\mu\cos\psi, \tag{3}$$

where ψ and θ_μ are the azimuthal angle and the tangent angle (half beam angle) in the magnetic field coordinate, respectively. Combine Equations (1), (2), and (3), we then obtain one-dimensional two-order differential equation for the acceleration potential, i.e.

$$\frac{{\rm d}^2\Psi}{{\rm d}\theta^2} - \frac{s_\theta^{''}}{s_\theta^{'}}\frac{{\rm d}\Psi}{{\rm d}\theta} = \frac{\Omega B_0 R^3}{cr^3}\sqrt{3\cos^2\theta+1}(\cos\zeta_{\rm out} - \cos\zeta)s_\theta^{'\,2}, \tag{4}$$

where $s_\theta^{'}$, $s_\theta^{''}$ are given by

$$s_\theta^{'} = \frac{{\rm d}s}{{\rm d}\theta} = \sqrt{r^2 + \left(\frac{{\rm d}r}{{\rm d}\theta}\right)^2},$$

$$s_\theta^{''} = \frac{{\rm d}s_\theta^{'}}{{\rm d}\theta},$$

$$r = R_{\rm e}\sin^2\theta,$$

here $R_{\rm e}$ is a field line constant, which denotes for the maximum length of a certain point on a field line. Then substituting $\tan\theta_\mu = \frac{3\tan\theta}{2-\tan^2\theta}$ (Qiao & Lin 1998) into Equations (3) and (4), we can solve the Equation (4) , and achieve the 1-D solution for the electric potential Ψ along a magnetic filed line with a magnetic azimuthal of $\psi = 0^\circ$ for the Crab pulsar, as shown in Figure 2. The maximum potential drop on this field line is comparable to the potential

$$\Delta V = \frac{\Omega B R^2}{2c} = 1.0 \times 10^{14} B_{12} R_6^2 P^{-1},$$

which is generated by the unipolar effect. The acceleration potential is quite huge in the inner region of annular gap, and the primary particles are therefore accelerated to ultra-relativistic energy with large Lorentz factors of $\gamma \sim 10^6 - 10^7$. Simultaneously, the accelerated primary particles emit abundant γ-ray photons through ICS and CR process, then dense $\mathrm{e}^{\pm}$ pairs are generated via $\gamma-$B (photon magnetic absorption) process.

2.3. *Pair Production*

Since ICS and curvature radiation are two effective radiation mechanisms to generate high energy γ-ray photons, $\mathrm{e}^{\pm}$ pairs can be generated by these ICS and CR photons emitted from the accelerated primary particles in both annular gap and core gap. Thus three gap modes exist for pair production, namely, CR gap, thermal ICS gap and resonant ICS gap (Zhang et al. 1997a,b), which will be briefly introduced below.

In the traditional inner gap model (Ruderman & Sutherland 1975), $\gamma - B$ process plays a very important role, two conditions should be satisfied at the same time for pair production: (1) to produce enough high energy γ-ray photons, a strong enough potential drop should be reached; (2) for pair production, the energy component of γ-ray photons perpendicular to the magnetic field must satisfy the condition of $E_{\gamma,\perp} \geq 2m_e c^2$.

The accelerated particles are assumed to flow along a field line in a quasi-steady state. Using the calculated acceleration electric field, we can obtain the Lorentz factor $\gamma_{\rm p}$ of the primary particle from the curvature radiation reaction

$$\gamma_{\rm p} = (\frac{3\rho^2 E_{\parallel}}{2e})^{\frac{1}{4}} = 2.36 \times 10^7 {\rho_7}^{0.5} E_{\parallel,\,6}^{0.25}, \tag{5}$$

where e is the charge of an electron, ρ_7 is the curvature radius in units of 10^7 cm and $E_{\parallel,\,6}$ is the acceleration electric field in units of $10^6 \mathrm{V\,cm^{-1}}$.

In $\gamma-$B process, the conditions for pair production are that the mean free path of γ-ray photon in strong magnetic field is equal to the gap height, $l \approx h$. The mean free path of γ-ray photon is given by (Erber 1966)

$$l = \frac{4.4}{e^2/\hbar c}\frac{\hbar}{m_e c}\frac{B_c}{B_\perp}\exp(\frac{4}{3\chi}), \tag{6}$$

where $B_{\rm c} = 4.414 \times 10^{13}$ G is the critical magnetic field, $\hbar$ is the reduced Planck's constant,

$$\chi = \frac{E_\gamma}{2m_e c^2}\sin\theta\frac{B}{B_{\rm c}} = \frac{E_\gamma}{2m_e c^2}\frac{B_\perp}{B_{\rm c}}, \tag{7}$$

and $B_\perp$ is the magnetic field perpendicular to the moving direction of γ photons, which can be expressed as (RS75)

$$B_\perp \approx \frac{h}{\rho}B \approx \frac{l}{\rho}B. \tag{8}$$

Here $l \approx h$ is the condition for gap sparks (pair production) to take place. ρ is curvature radius of a spot on a magnetic field line. For a dipole magnetic configuration, it can be estimated as

$$\rho \approx \frac{4}{3}(\lambda R c/\Omega)^{1/2} \tag{9}$$

(Zhang et al. 1997b) if the spot position is near the neutron star surface. Here λ is a parameter to show the field lines, $\lambda = 1$ corresponding to the last open field line. The characteristic energy from the curvature radiation process can be written as

$$E_{\gamma,cr} = \hbar\frac{3\gamma^3 c}{2\rho}. \tag{10}$$

Then the CR gap height $h_{\rm CR}$ is

$$h_{\rm CR} \simeq 5 \times 10^3 P^{3/7} B_{12}^{-4/7} \rho_6^{2/7}\ \mathrm{cm} \tag{11}$$

(Zhang et al. 1997b).

The so-called CR-mode gap implicates that the pair production cascades are dominated by the γ-ray photons emanated from curvature radiation process of the accelerated primary particles, this gap is somehow like the RS gap (Ruderman & Sutherland 1975). The resonant ICS gap is formed from the resonant scattering of soft photons, which is a quantum effect with a large electron scattering cross section estimated as $\sigma \sim 10^8 \sigma_{\rm T}$ ($\sigma_{\rm T}$ is the Thompson cross section) in strong magnetic fields. Zhang et al. (1997b) obtained the gap height ($h_{\rm res}$) of the resonant ICS mode

$$h_{\rm res} \simeq 1.1 \times 10^3 P^{1/3} B_{12}^{-1} \rho_6^{1/3}\ \mathrm{cm}, \tag{12}$$

and the Lorentz factor ($\gamma_{2,\,\rm res}$) of pairs for the resonant ICS mode

$$\gamma_{2,\,\rm res} = 890 P^{-1/3} B_{12} \rho_6^{2/3}. \tag{13}$$

The thermal ICS gap is determined by those thermal-peak photons which has the maximum photon number density of the Planck spectrum at a certain temperature. It has a lower gap height $h_{\rm th}$

$$h_{\rm th} = 2.7 \times 10^2 P^{2/5} B_{12}^{-3/5} \rho_6^{1/5} T_6^{-1/5}\ \mathrm{cm}, \tag{14}$$

but lead to a larger Lorentz factor ($\gamma_{2,\,\rm th}$) for the secondary particles

$$\gamma_{2,\,\rm th} = 3.7 \times 10^3 P^{-2/5} B_{12}^{3/5} \rho_6^{4/5} T_6^{1/5} \tag{15}$$

(Zhang et al. 1997b).

These two CR and ICS gaps, which have relatively lower gap heights, would dominate the inner gap breakdown (Zhang et al. 1997b; Du et al. 2009). The pairs can also be abundantly generated by the primary particles escaped from the inner gap within a few neutron star radii, and they could have two major energy distributions due to the different types of primary particles. We will therefore use two different pair energy distributions for CR and ICS pairs to calculate the phase-averaged spectrum and phase-resolved spectra for the Crab pulsar.

3. MODELING THE MULTI-WAVELENGTH LIGHT CURVES AND SPECTRA FOR THE CRAB PULSAR

To explain the multi-wavelength light curves with nearly aligned peak phase for the Crab pulsar, we should obtain the high signal-to-noise data, which are adopted from Figure 2 of (Abdo et al. 2010). We also reprocessed the *Fermi* γ-ray data to obtain the three γ-ray band light curves (see left panels of Figure 3) in the following steps:

1. Limited by the timing solution for the Crab pulsar[3] from the Fermi Science Support Center (FSSC), we reprocessed the original data observed from 2008 August 4 to 2009 April 8.

---

[3] http://fermi.gsfc.nasa.gov/ssc/data/access/lat/ephems/

2. We selected photons of 0.1-300 GeV in the "Diffuse" event class, within a radius of 2° of the Crab pulsar position (RA= 83.63°, DEC= 22.01°) and the zenith angle smaller than 105°.

3. As done by Abdo et al. (2010), we used "fselect" to select photons of energy $E_{\rm GeV}$ within an angle of $< \max\,[\,6.68 - 1.76\log_{10}(E_{\rm GeV}), 1.3\,]$ degrees from the pulsar position.

4. We then obtained the rotational phase for each photon using the tempo2 (Hobbs et al. 2006) with the *Fermi* plug-in.

5. Finally we obtained the multi-wavelength γ-ray light curves with 256 bins, as presented in Figure 3 (left panels). Two sharp phase-aligned peaks have a phase separation of $\delta\phi \sim 0.4$.

An acceptable model should have reasonable input parameters (e.g., magnetic inclination angle α and viewing angle ζ), and consistently produce multi-wavelength light curves with phase-aligned peaks and bridge emission and phase-resolved spectra for the Crab pulsar .

3.1. *Light Curves Modeling*

We adopted the method (see details in §3.1 of Du et al. 2011, including basic formulae and gap physics) to model the light curves. The key idea of modeling light curves is to project the radiation intensity of every spot on each open filed line (in either annular gap or core gap) to the "non-rotating" sky, with considerations of physical effects. Here the emissivities are numerically assumed to facilitate calculations, they are however consistent with the physically calculated spectra, as noted in Figure 8 of Du et al. (2011). Some model parameters for both the annular gap and core gap should be adjusted for the emission regions where the corresponding waveband emission are generated. The framework of the annular gap model as well as the details of coordinate system have been presented in Du et al. (2010), which can be used for simulation of the multi-wavelength light curves of the Crab pulsar. We adopted the inclination angle of $\alpha = 45^\circ$ and the viewing angle $\zeta = 63^\circ$ which were obtained from the *Chandra* X-ray torus fitting (Ng & Romani 2008). The modeling methods are briefly delineated as follows.

1. We first use the critical field line to separate the polar cap region into the annular and core gap regions. Then we use the so-called "open volume coordinates" ($r_{\rm OVC}, \psi_{\rm s}$) to label the open field lines of the annular gap and core gap, respectively. Here $r_{\rm OVC}$ is the normalized magnetic colatitude and $\psi_{\rm s}$ is the magnetic azimuthal. For the annular gap, we define the inner rim $r_{\rm OVC,\,AG} \equiv 0$ for the critical field lines and the outer rim $r_{\rm OVC,\,AG} \equiv 1$ for the last open field lines; while for the core gap, We define the outer rim $r_{\rm OVC,\,CG} \equiv 1$ for the critical field lines and the inner rim $r_{\rm OVC,\,CG} \equiv 0$ for the magnetic axis. We also divide both the annular gap ($0 \lesssim r_{\rm OVC,\,AG} \lesssim 1$) and the core gap ($0.1 \lesssim r_{\rm OVC,\,CG} \lesssim 1$) into 40 rings for calculation.

2. When calculating the emissivities for modeling light curves, we postulate that the emissivities along one open field line have a Gaussian distribution rather than the frequently used assumption of the uniform emissivity along an open field line (Dyks & Rudak 2003; Fang & Zhang 2010) for both the annular gap and the core gap. To justify this key assumption, we already used the realistic acceleration field to plot the flux against emission altitude along an open field line for the Vela, as shown in Fig. 8 of Du et al. (2011). From that figure, one can clearly see that the flux is likely to have a Gaussian distribution against altitude near the peak position. The peak emissivities $I_{\rm p}(\theta_{\rm P}, \psi_{\rm s})$ may follow another Gaussian distribution against θ for a bunch of open field lines (Cheng et al. 2000; Dyks & Rudak 2003; Fang & Zhang 2010). As seen above, we use two different Gaussian distributions to describe the emissivities on open field lines for both the annular gap and the core gap. The model parameters are adjusted to maximally fit the observed multi-wavelength light curves.

3. To derive the "photon sky-map" in the observer frame, we first calculate the emission direction of each emission spot $\mathbf{n}_{\rm B}$ in the magnetic frame; then use a transformation matrix T_α to transform $\mathbf{n}_{\rm B}$ into $\mathbf{n}_{\rm spin}$ in the spin frame; finally use an aberration matrix to transform $\mathbf{n}_{\rm spin}$ to $\mathbf{n}_{\rm observer} = \{\mathbf{n}_{\rm x},\, \mathbf{n}_{\rm y},\, \mathbf{n}_{\rm z}\}$ in the observer frame. Here $\phi_0 = \arctan(\mathbf{n}_{\rm y}/\mathbf{n}_{\rm x})$ and $\zeta = \arccos(\mathbf{n}_{\rm z}/\sqrt{{\mathbf{n}_{\rm x}}^2 + {\mathbf{n}_{\rm y}}^2 + {\mathbf{n}_{\rm z}}^2})$ are the rotation phase (without retardation effect) of the emission spot with respect to the pulsar rotation axis and the viewing angle for a distant, nonrotating observer. The detailed calculations for the aberration effect can be found in Lee et al. (2010).

4. We also add the phase shift $\delta\phi_{\rm ret}$ caused by the retardation effect to the emission phase, that is $\phi = \phi_0 - \delta\phi_{\rm ret}$. There is no minus sign for ϕ_0 because of our coordinate system different from other models.

5. The "photon sky-map", defined by the binned projected emission intensities on the (ϕ, ζ) plane, can be plotted in 256 bins (see middle panel of Figure 3). The corresponding light curves cut by a line of sight with a viewing angle $\zeta = 63^\circ$ are finally obtained. For the viewing angle $\zeta = 63^\circ$, any magnetic inclination angles of α between 40° and 65° in the annular gap model can produce light curves with two peaks and a large peak separation similar to the observed ones. The emission from the single pole is favored for the Crab pulsar in our model.

The modeled light curves from radio to TeV band are presented in Figure 3 (black solid lines), and the key model parameters are listed in Table 1. Emission from P1 and P2 of multi-wavelength light curves originates from the annular gap region in the vicinity of the null charge surface, while bridge emission comes from the core gap region. We emphasize that all the multi-wavelength emission are originated from only one magnetic pole, our annular gap is therefore a single-pole magnetospheric model.

With well-coordinated efforts for pulsar radio timing program, Abdo et al. (2010) determined the phase lag between radio emission and γ-ray light curves. The first γ-ray peak comes earlier than the 1.4 GHz radio pulse by a small phase of ~ 0.00853, but they are nearly phase-aligned. From light curve modeling, we can obtain the emission locations for each

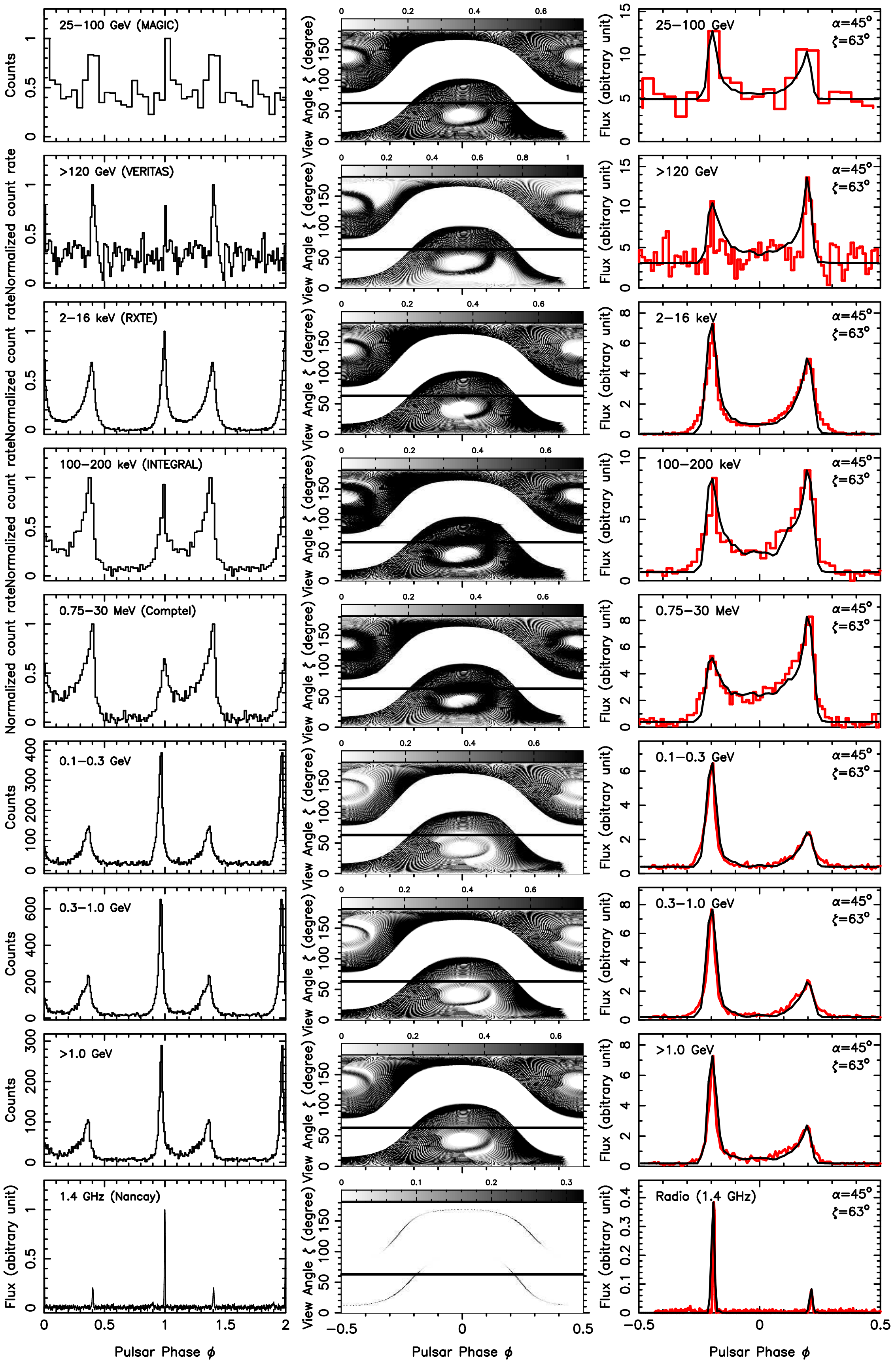

FIG. 3.— Multi-wavelength (radio, X-ray and γ-ray) light curves for the Crab pulsar. The observations are shown in the left panels, and the data of RXTE, INTEGRAL, Comptel and Nancay are taken from Figure 2 of Abdo et al. (2010). The 25−100 GeV light curve data are taken from Aleksić et al. (2011), and the TeV ($>$120 GeV) data are taken from VERITAS Collaboration et al. (2011). The photon sky-map (middle panels) for an inclination angle and the corresponding modeled light curves (right panels) for a viewing angle of $\zeta = 63^\circ$ are also presented, using the single-pole annular gap model. Our annular gap model can well explain the multi-wavelength light curves with phase-aligned peaks.
(A color version of this figure is available in the online journal.)

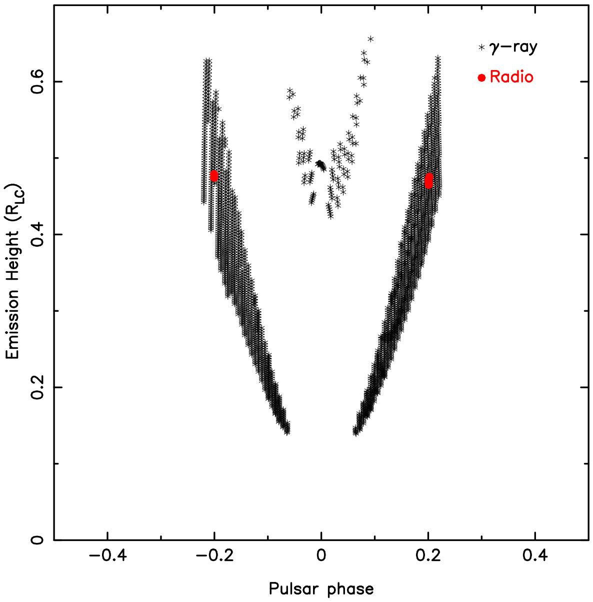

FIG. 4.— γ-ray and radio emission altitudes for the Crab pulsar with a viewing angle $\zeta = 63^\circ$ in the annular gap model. The γ-ray peak and radio (1.4 GHz) emission altitudes are nearly overlapped in the annular gap region, which leads to the phase-aligned peaks of the two energy band. While bridge emission are generated from the core gap region.
(A color version of this figure is available in the online journal.)

TABLE 1
MODEL PARAMETERS FOR MULTI-WAVELENGTH LIGHT CURVES OF THE CRAB PULSAR

Band	κ	λ	ϵ	$\sigma_{\rm A}$	$\sigma_{\theta,\,\rm A}$	$\sigma_{\rm C}$	$\sigma_{\theta,\,\rm C1}$	$\sigma_{\theta,\,\rm C2}$
25–100 GeV	0.65	0.6	0.8	0.4	0.0045	0.25	0.0023	0.0035
$>$120 GeV	0.68	0.85	0.8	0.3	0.0035	0.25	0.0025	0.0032
2–16 keV	0.50	0.8	1.17	0.5	0.005	0.3	0.0022	0.0035
100-200 keV	0.50	0.8	0.8	0.6	0.006	0.35	0.0035	0.0045
0.75-30 MeV	0.52	0.8	0.7	0.5	0.004	0.3	0.005	0.006
0.1–0.3 GeV	0.53	0.8	0.6	0.5	0.004	0.15	0.0012	0.0012
0.3–1.0 GeV	0.54	0.8	0.7	0.5	0.005	0.15	0.0014	0.0014
$>$1.0 GeV	0.57	0.8	0.5	0.5	0.005	0.35	0.0035	0.0035

Note. κ and λ are two geometry parameters to determine the peak altitude in the annular gap; ϵ is a parameter for the peak altitude in the core gap; $\sigma_{\rm A}$ and $\sigma_{\rm C}$ are length scales for the emission region on each open field line in the annular gap and the core gap in units of $R_{\rm LC}$, respectively; $\sigma_{\theta,\,\rm A}$ is the transverse bunch scale for field lines in the annular gap; $\sigma_{\theta,\,\rm C1}$ and $\sigma_{\theta,\,\rm C2}$ are the bunch scale for field lines of $-180^\circ < \psi_{\rm s} < 90^\circ$ and $90^\circ < \psi_{\rm s} < 180^\circ$ in the core gap, respectively. The detailed description of these symbols can be found in (Du et al. 2011).

band. The result of γ-ray and radio emission altitudes for the Crab pulsar is shown in Figure 4. The region for the radio emission is mainly located at a altitude of $\sim 0.5 R_{\rm LC}$ on some certain filed lines, for P1, the magnetic azimuthal ψ is in the range of -98° to -96°, while 106° to 109° for P2. It is generated in an intermediate-altitude annular gap region, which might be due to the coherence condition and propagation effects. It is found that the positions of both γ-ray (X-ray) peak and radio peak (1.4 GHz) are overlapped, this leads to the nearly phase-aligned pulse peaks of multi-wavelength emission, except for several GHz radio emission due possibly to plasma propagation effects. Nevertheless, the γ-ray emission altitudes are above the lower bound of the height determined by $\gamma - B$ absorption (Lee et al. 2010). Based on our model, not all γ-ray pulsars can be detected in the radio band, and not all radio pulsars can have a γ-ray beam with sufficiently high flux towards us. The beam shapes and intensities of $\gamma{-}$ray and radio can evolve with pulsar ages.

3.2. *Multi-wavelength Spectra for the Crab Pulsar*

In this section, we will use the annular gap model to calculate the multi-wavelength phase-averaged spectrum and phase-resolved spectra for the Crab pulsar. Kuiper et al. (2001) achieved seven band phase-resolved spectra (LW1, P1, TW1, Bridge, LW2, P2, TW2) and the phase-averaged spectrum of the Crab pulsar with the *EGRET* γ-ray data. We will also add the new high-quality *Fermi*, MAGIC and VERITAS data to the total phase-averaged spectrum. The γ-ray emission is believed to be originated from the curvature radiation of primary particles (Tang et al. 2008; Harding et al. 2008; Meng et al. 2008), which generally gives a super-exponential power-law spectrum with the cut-off energy of a few GeV. However, the TeV (20 to 400 GeV) emission mechanism remains a mystery, and it requires a global phase-averaged spectrum fitting to resolve this problem.

We first discuss the particle dynamics in the annular gap. After exploring the formation mechanism of acceleration electric field, the relevant dynamic parameters: acceleration electric field $E_{\parallel}$, Lorentz factor of primary particles $\gamma_{\rm p}$, characteristic energy of curvature radiation emitted from primary particles $E_{\rm C}$ and escape photon energy $E_{\rm es}$ are calculated for two field lines where P1 and P2 are mainly originated. The calculated results are shown in Figure 5. As introduced in § 2.2, the derived acceleration electric field $E_{\parallel}$ is quite huge in the inner region of annular gap below the altitude of $R_{\rm lim}$, which leads to the generation of numerous pairs via $\gamma{-}$B absorption effect. The Lorentz factor of primary particles $\gamma_{\rm p}$ is derived from the curvature radiation reaction using the Equation (5). However, the actual Lorentz factor of the primary particles is smaller than the one shown in Figure 5 if other energy loss mechanisms (e.g. ICS loss rate) as well as relativistic and pair screening effects are taken into account. $E_{\rm C}$ denotes for the characteristic energy of curvature radiation emitted from primary particles, derived by the Equations (5) and (10). $E_{\rm es}$, due to the $\gamma{-}$B absorption effect based on the Equation (26), is the escape (maximum) photon energy for a certain altitude.

We will further consider the emission mechanisms for the Crab pulsar. The photon number spectrum of the synchrotron radiation is given by

$$\left(\frac{{\rm d}^2 N_\gamma}{{\rm d}E_\gamma {\rm d}t}\right)_{\rm syn} = \frac{\sqrt{3} e^3 B(r) \sin\varphi(r)}{m_e c^2 h} \frac{1}{E_\gamma} G(x), \qquad (16)$$

where $\varphi(r)$ is the pitch angle at a distance of r on an open field line, h is the Planck constant, $G(x) = x \int_x^\infty K_{\frac{5}{3}}(\xi) d\xi$, $K_{\frac{5}{3}}$ is the modified Bessel function with an order of $5/3$, $x = E_\gamma / E_{\rm syn,\,c}(r)$ and

$$\begin{aligned} E_{\rm syn,\,c}(r) &= 1.5 h \gamma^2 \nu_{\rm L} \sin\varphi(r) \\ &= 4.3 \times 10^6 h B(r) \gamma^2 \sin\varphi(r) \qquad (17) \end{aligned}$$

is the critical synchrotron photon energy. The pitch angle $\varphi(r)$ of relativistic primary particles flowing along a magnetic field line could be small, but it cannot be neglected for synchrotron radiation. While the pitch angle $\varphi(r)$ of pairs increases due to the cyclotron resonant absorption of the low-energy photons (Harding et al. 2008) and it varies with the emission altitudes. The mean pitch angles of the two types of pairs are different owing to the effect of cyclotron resonant

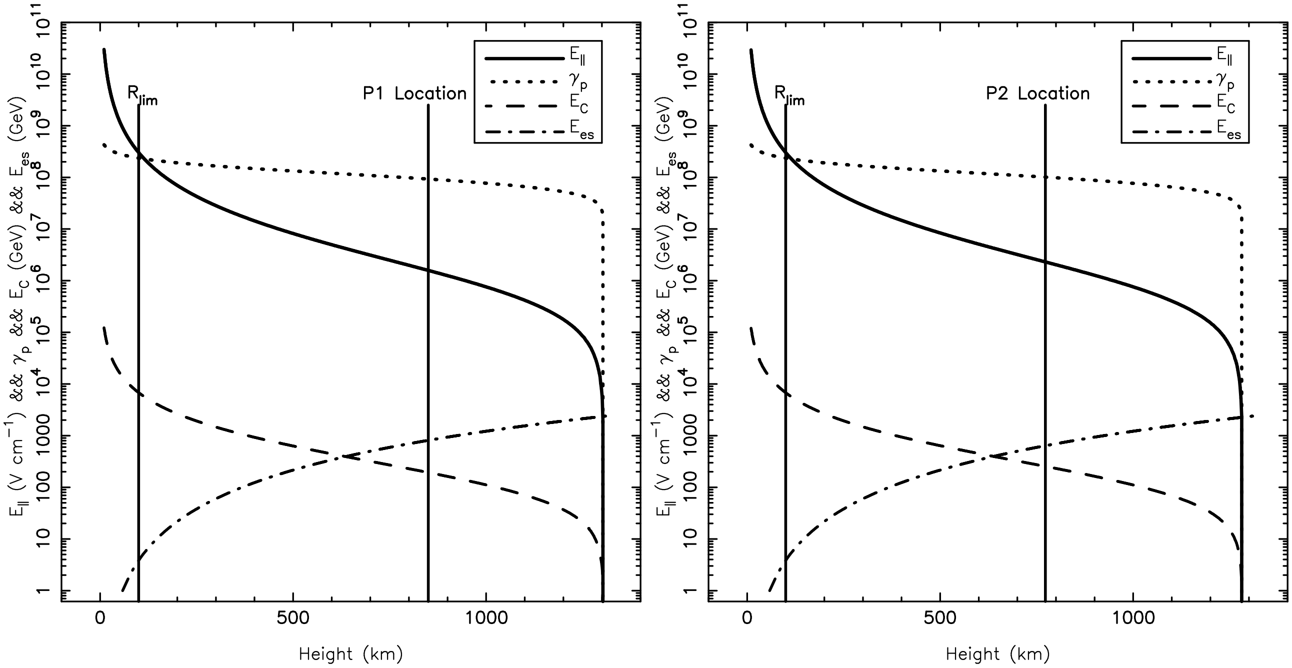

FIG. 5.— Four dynamic parameters along two open field lines where P1 (top panel) and P2 (bottom panel) are mainly originated. The acceleration electric field $E_{\parallel}$ (solid line) is quite huge in the inner region of annular gap below the altitude of $R_{\rm lim}$, which results in the generation of numerous pairs. The Lorentz factor of primary particles $\gamma_{\rm p}$ (dotted line) is derived from the curvature radiation reaction. $E_{\rm C}$ (dashed line) denotes for the characteristic energy of curvature radiation emitted from primary particles. $E_{\rm es}$ (dot-dash line) is the escape (maximum) photon energy for a certain altitude due to the $\gamma-$B absorption.

absorption for different particles with different Lorentz factors. The synchrotron radiation from pairs play an important role in X-ray band to soft γ-ray band (e.g. $\lesssim 0.02$ GeV).

The photon number spectrum of the curvature radiation can be given by

$$\left(\frac{{\rm d}^2N_\gamma}{{\rm d}E_\gamma {\rm d}t}\right)_{\rm cur} = \frac{\sqrt{3}e^2\gamma}{h\rho(r)E_\gamma}G(x), \tag{18}$$

where $\rho(r)$ is the curvature radius at r and Equation (10) shows the critical curvature photon energy.

Blumenthal & Gould (1970) presented an analytic formula for the photon spectrum of the inverse Compton scattered photons per electron in the case of extreme Nishia-Klein limit and then Tang et al. (2008) gave a simplified form, i.e.,

$$\begin{aligned}\left(\frac{{\rm d}^2N_\gamma}{{\rm d}E_\gamma {\rm d}t}\right)_{\rm ICS} = &\int_{\varepsilon_1}^{\varepsilon_2} \frac{3\sigma_{\rm T}c}{4\gamma^2}\cdot\frac{n_{\rm syn}(\varepsilon,r)+n_{\rm X}(\varepsilon,r)}{\varepsilon} \\ &\times\left[2q\ln q+(1+2q)(1-q)+\frac{(\Gamma q)^2(1-q)}{2(1+\Gamma q)}\right]{\rm d}\varepsilon, \end{aligned}\tag{19}$$

where $q = E_1/\Gamma(1-E_1)$, $\Gamma = 4\gamma\varepsilon/m_ec^2$ and $E_1 = E_\gamma/E_e$. ε is the energy of soft photons for scattering, and ε_1 and ε_2 are the minimum and maximum energy of the soft photons for integration, respectively. We choose the values of ε_1 and ε_2 to fulfill the condition of $E_1 < 1$. The lower limit ε_1 in the Equation(19) is chosen to be around 1 eV, and the upper limit ε_2 is adjusted artificially to make a quick convergence of the Equation(19).

There are two possible sources of soft photons for the inverse Compton scattering, one is the thermal photons, and the other is synchrotron photons. The thermal photons, generated by the stellar surface with a typical surface temperature T, is an important source for Compton scattering of the primary particles and secondary particles. The number density of soft photons is given by

$$n_{\rm X}(\varepsilon,r) = \frac{1}{\pi^2(\hbar c)^3}\frac{\varepsilon^2}{\exp(\varepsilon/kT)-1}\left(\frac{R}{r}\right)^2, \tag{20}$$

where k is the Boltzmann constant. The temperature T is taken to be 2×10^6 K in our calculations.

The other source of soft photons arises from synchrotron radiation of pairs. Owing to the quite abundant soft synchrotron photons, the scattering of this kind of photons is more significant at higher altitudes near the light cylinder. Although the synchrotron radiation spectrum from a single particles with a Lorentz factor of γ is maintained to a wide energy band (for example, soft X-ray band to γ-band), it is more likely to be a spectral line in fact, which is concentrated on the critical energy. Thus we can rewrite the synchrotron spectral power using the total energy loss rate, i.e.,

$$P_{\nu,\,{\rm syn}} \simeq \dot{E}_{\rm syn}\delta(\varepsilon-\varepsilon_{\rm syn,\,c}) \simeq \frac{4}{3}\sigma_{\rm T}cU_{\rm B}\gamma^2\delta(\varepsilon-\varepsilon_{\rm c}), \tag{21}$$

where $\sigma_{\rm T}$ is the Thompson scattering cross section, $U_{\rm B}$ is the energy density of the local magnetic field, and $\delta(\varepsilon-\varepsilon_{\rm c})$ is a Delta function.

Supposing pairs follow a power-law spectrum $n_{\rm e}(\gamma) = n_0\gamma^{-s}$ with a particle energy spectral index of s, we can obtain the synchrotron emissivity j_ν in a simple form

$$j_\nu = \frac{1}{\Delta\Omega}\int P_{\nu,\,{\rm syn}}n_{\rm e}(\gamma){\rm d}\gamma = \frac{2\sigma_{\rm T}cU_{\rm B}n_0}{3\Delta\Omega\nu_{\rm L}}\left(\frac{\nu}{\nu_{\rm L}}\right)^{\frac{1-s}{2}}, \tag{22}$$

where $\nu_{\rm L}$ is the Larmor frequency of an electron in the magnetic field, n_0 is a constant and $\Delta\Omega(r)$ is the solid angle of the beam of synchrotron photons and is estimated as

$$\Delta\Omega(r) = \int_0^{2\pi}\int_0^{\varphi(r)} d\phi\sin\theta d\theta \approx \pi\varphi^2(r). \tag{23}$$

TABLE 2
BEST FIT PARAMETERS FOR THE CALCULATED PHASE-AVERAGED SPECTRUM OF THE CRAB PULSAR

α	ζ	$\gamma^{\rm CR}_{\rm min,\,pair}$	$\gamma^{\rm CR}_{\rm max,\,pair}$	$\varphi^{\rm CR}_{\rm pair}$	$\gamma^{\rm ICS}_{\rm min,\,pair}$	$\gamma^{\rm ICS}_{\rm max,\,pair}$	$\varphi^{\rm ICS}_{\rm pair}$	$\gamma^{\rm pri}_{\rm min}$	$\gamma^{\rm pri}_{\rm max}$	$\varphi_{\rm pri}$
45°	63°	2.5×10^2	2.18×10^4	0.0092	6.0×10^2	1.19×10^5	0.0074	1.0×10^6	2.78×10^7	0.000098

TABLE 3
BEST FIT PARAMETERS FOR THE CALCULATED PHASE-RESOLVED SPECTRA OF THE CRAB PULSAR

Phase band	$\gamma^{\rm CR}_{\rm min,\,pair}$	$\gamma^{\rm CR}_{\rm max,\,pair}$	$\varphi^{\rm CR}_{\rm pair}$	$\gamma^{\rm ICS}_{\rm min,\,pair}$	$\gamma^{\rm ICS}_{\rm max,\,pair}$	$\varphi^{\rm ICS}_{\rm pair}$	$\gamma^{\rm pri}_{\rm min}$	$\gamma^{\rm pri}_{\rm max}$	$\varphi_{\rm pri}$	$\Delta\Omega_{\rm eff}$
LW1	2.5×10^2	1.2×10^4	0.009	—	—	—	1.0×10^6	1.76×10^7	0.00005	1.82
P1	2.5×10^2	0.9×10^4	0.0078	4.6×10^2	0.86×10^5	0.0071	1.0×10^6	2.47×10^7	0.00009	3.03
TW1	2.5×10^2	0.95×10^4	0.009	3.0×10^2	0.68×10^5	0.0079	1.0×10^6	2.78×10^7	0.00008	3.16
Bridge	3.0×10^2	0.71×10^4	0.0085	5.0×10^2	0.55×10^5	0.0070	1.0×10^6	2.55×10^7	0.00003	2.53
LW2	3.5×10^2	1.25×10^4	0.008	5.0×10^2	0.52×10^5	0.0079	1.0×10^6	2.50×10^7	0.00005	1.78
P2	5.0×10^2	1.22×10^4	0.0078	5.0×10^2	0.82×10^5	0.0085	1.0×10^6	2.97×10^7	0.000072	3.81
TW2	5.0×10^2	1.3×10^4	0.008	—	—	—	1.0×10^6	1.82×10^7	0.00007	2.78

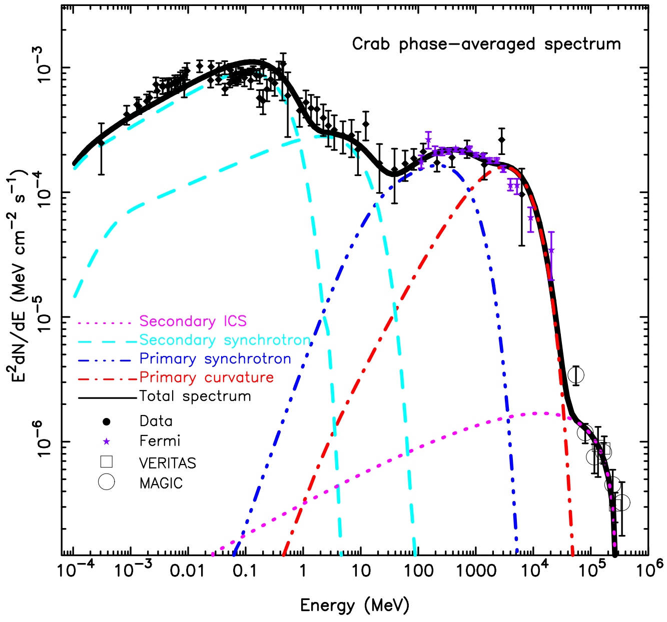

FIG. 6.— The modeled phase-averaged spectrum for the Crab pulsar. The calculated total spectrum (thick black solid line) is obtained from the sum of synchrotron radiation and ICS from two kinds of pairs and curvature radiation and synchrotron radiation from primary particles. It is found that the curvature radiation and synchrotron radiation from primary particles is mainly contributed to γ-ray band (20 MeV to 20 GeV); synchrotron radiation from CR-induced pairs and ICS-induced pairs dominates the X-ray band and soft γ-ray band (100 eV to 10 MeV). ICS from the pairs contributes to hard TeV γ-ray band ($\sim$ 20 GeV to 400 GeV). The data (solid circles) are taken from Kuiper et al. (2001). The *Fermi* γ-ray data is plotted in purple circles. The γ-ray spectral data of VERITAS (square) are taken from VERITAS Collaboration et al. (2011), and the MAGIC data (big hollow circle) are taken from MAGIC Collaboration et al. (2012).
(A color version of this figure is available in the online journal.)

Therefore we use an approximate formula to facilitate ICS calculations when we consider the soft seed synchrotron photons. The number density of the soft synchrotron photons, $n_{\rm syn}(\varepsilon, r)$ can be given by

$$n_{\rm syn}(\varepsilon, r) = \frac{\Delta\Omega r}{hc\varepsilon} j_\nu = \frac{2\sigma_{\rm T} U_{\rm B} n_0 r}{3\varepsilon_{\rm L}^2}\left(\frac{\varepsilon}{\varepsilon_{\rm L}}\right)^{-\frac{1+s}{2}}, \quad (24)$$

where $\varepsilon_{\rm L} = h\nu_{\rm L}$ is the Larmor energy.

Following the method of Du et al. (2011), we divide the annular gap region into 40 rings and 360 equal intervals in the magnetic azimuth, i.e. in total 40×360 small magnetic tubes. A small magnetic tube has an area A_0 on the neutron star surface. From Equation (2), the number density of primary particles at a altitude r is $n(r) = \frac{\Omega B(r)}{2\pi c\ e}\cos\zeta_{\rm out}$. The cross-section area of the magnetic tube at r is $A(r) = B_0 A_0/B(r)$. The flowing particle number at r in the magnetic tube is

$$\Delta N(r) = A(r)\Delta s \frac{\Omega B(r)}{2\pi c e}\cos\zeta_{\rm out}, \quad (25)$$

here Δs is the arc length along the field. The energy spectrum $N_{\rm pri} = {\rm d}N/{\rm d}\gamma$ of the accelerated primary particles is not well understood in the first physical principle. Here we assume the primary particles in the magnetic tube to follow a power-law energy distribution ${\rm d}N/{\rm d}\gamma = N_0\gamma^\Gamma$ with an index of $\Gamma = -2.2$. Using Equation (25), N_0 can be derived by integration the equation above.

Harding et al. (2008) have assumed a broken power-law distribution for pairs with indexes of -2.0 and -2.8 [see their Equation (47)]. But in our model, we postulate that the two types of relativistic pairs follow two different power-law energy distribution as noted in § 2.3, i.e.

$$N_{\rm pairs}(\gamma) = \begin{cases} C_1\gamma^{-s_1}, \ \gamma^{\rm CR}_{\rm min} \leqslant \gamma \leqslant \gamma^{\rm CR}_{\rm max}, \\ C_2\gamma^{-s_2}, \ \gamma^{\rm ICS}_{\rm min} \leqslant \gamma \leqslant \gamma^{\rm ICS}_{\rm max}, \end{cases}$$

where $s_1 = 2.45$ and $s_2 = 2.6$ are the spectral index, C_1 and C_2 are two coefficients, $\gamma^{\rm CR}_{\rm min}$, $\gamma^{\rm CR}_{\rm max}$, $\gamma^{\rm ICS}_{\rm min}$ and $\gamma^{\rm ICS}_{\rm max}$ are lower limits and upper limits of the Lorentz factors for the CR and ICS pairs.

The pairs can be generated with a large multiplicity (10^3-10^5) via the $\gamma - B$ process in the lower regions of the annular gap and the core gap near the neutron star surface. The pitch angle of pairs increases due to the cyclotron resonant absorption of the low-energy photons. The mean pitch angle of secondary particles is considerable owing to the effect of cyclotron resonant absorption. The synchrotron radiation from secondary particles has some contributions to the low-energy γ-ray emission, e.g. $\lesssim 0.02$ GeV.

We also had an analytical formula of optical depth $\tau_{\gamma-{\rm B}}$ due to the γ−B absorption (Lee et al. 2010)

$$\tau_{\gamma-{\rm B}}(r) = \frac{1.55\times10^7 r}{E_\gamma} K^2_{1/3}(\frac{2.76\times10^6 r^{5/2} P^{1/2}}{B_{0,\,12} R^3 E_\gamma}), \quad (26)$$

here E_γ is in units of MeV, $B_{0,\,12}$ is the surface magnetic field in units of 10^{12} G. We found that the photons of the Crab pul-

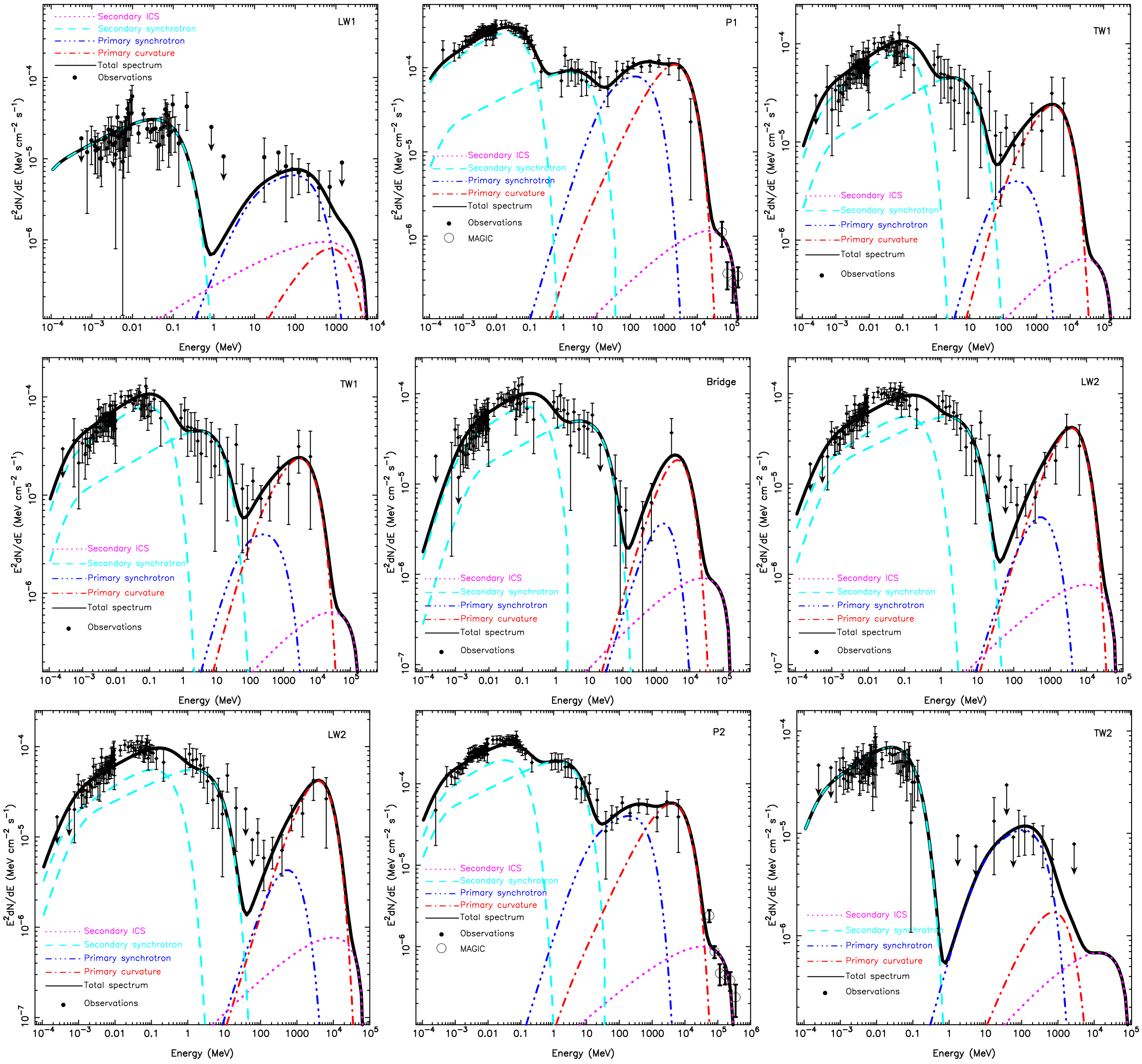

FIG. 7.— Similar as Figure 6, but for modeled seven phase-band phase-resolved spectra of the Crab pulsar. TW1 and LW2 are plotted twice. The MAGIC (50−400 GeV) spectral data are available only for P1 and P2, which are taken from MAGIC Collaboration et al. (2012), whereas the *Fermi* and VERITAS data are not included here.
(A color version of this figure is available in the online journal.)

sar with an energy of $< 100\,$GeV always satisfy the condition of $\tau_{\gamma-{\rm B}} \ll 1$ if the emission altitude is greater than a few hundred kilometers. Thus the final multi-wavelength spectrum emitted by the primary particles and secondary particles can be calculated by

$$F(E_\gamma)=\frac{1}{\Delta\Omega_{\rm eff}D^2}\int_{\gamma_{\rm min}}^{\gamma_{\rm max}}\left[\left(\frac{{\rm d}^2N_\gamma}{{\rm d}E_\gamma{\rm d}t}\right)_{\rm cur}+\left(\frac{{\rm d}^2N_\gamma}{{\rm d}E_\gamma{\rm d}t}\right)_{\rm syn}+\left(\frac{{\rm d}^2N_\gamma}{{\rm d}E_\gamma{\rm d}t}\right)_{\rm ICS}\right]e^{-\tau_{\gamma-{\rm B}}(r)}, \tag{27}$$

where $\Delta\Omega_{\rm eff}$ is the effective solid angle of the emission beam, and $D = 2\,$kpc is the distance from the Crab pulsar to the Earth.

There are actually six main spectral components for the pulsar total spectrum. Based on our calculations, the synchrotron and curvature radiation from primary particles and the synchrotron radiation and ICS from secondary particles are required to calculate the phase-averaged and phase-resolved spectra, while ICS from primary particles and CR from pairs can be ignored for the Crab pulsar. When we calculate the SR spectra, we carefully deal with the modified Bessel function with for unprecedent accuracies. While calculating ICS spectrum, as stated above, we use Equations (19) and (20) and (24) to reduce the computation time.

To accelerate our computations, we use the method of "averaged emission-altitude" (as introduced in Du et al. 2011) to calculate the four contributive spectral components for the Crab pulsar, i.e., synchrotron and curvature radiation from primary particles, and ICS and synchrotron radiation from pairs. We first obtain the emission altitudes from Figure

(4) for each phase band. For instance, the emission altitude is about $0.54\,R_{\rm LC}$ on the field line of a magnetic azimuth $\psi = -101^{\circ}$ for P1; while for P2, the emission altitude is $0.49\,R_{\rm LC}$ on the field line of $\psi = 109^{\circ}$. Then we compute their acceleration electric field $E_{\parallel}$ and potential Ψ, and adjust the minimum and maximum Lorentz factor for both primary particles and pairs ($\gamma_{\rm min}^{\rm pri}$ and $\gamma_{\rm max}^{\rm pri}$ and $\gamma_{\rm min}^{\rm 2nd}$ and $\gamma_{\rm max}^{\rm 2nd}$), the pitch angle $\varepsilon(r)$ and the γ-ray beam angle $\Delta\Omega_{\rm eff}$ to fit the multi-wavelength phase-averaged spectrum and phase-resolved spectra for the Crab pulsar.

We fitted the phase-averaged spectrum and seven phase-band phase-resolved spectra of the Crab pulsar, and the results are shown in Figure 6 and Figure 7, respectively. For phase-averaged spectrum, we basically used the multi-wavelength data from Kuiper et al. (2001) and combined with latest *Fermi*, MAGIC and VERITAS γ-ray spectral data, whereas for phase-resolved spectra, we only used the multi-wavelength data from Kuiper et al. (2001). The best fit parameters for phase-averaged spectrum and phase-resolved spectra are listed in Table 2 and Table 3, respectively. From spectra fitting, we found that the calculated γ-ray spectra are not sensitive to $\gamma_{\rm min}^{\rm pri}$, but quite sensitive to $\gamma_{\rm max}^{\rm pri}$ which is chosen below the value obtained from the balance of curvature radiation and radiation reaction shown in Figure 5. The solid angle $\Delta\Omega_{\rm eff}$ was always assumed to be 1 by many authors for simplicity. We adjusted it as a free parameter around 1 for different phases.

We found that multi-wavelength emission from the phase bands of P1, P2 and bridge contribute significantly to the total phase-averaged spectrum. The phase-averaged spectrum and phase-resolved spectra are decomposed into four spectral components. Curvature radiation and synchrotron radiation from primary particles is the main origin of the observed γ-ray emission (10 MeV to $\sim 20\,$GeV), synchrotron radiation from CR-induced pairs and ICS-induced pairs dominates the X-ray band and soft γ-ray band. ICS from the pairs contributes significantly up to TeV band, while ICS from both primary particles and curvature radiation from pairs can be neglected for the spectrum fitting. Owing to the larger emission altitudes (which leads to lower acceleration electric field) for LW1 and TW2, the lorentz factors γ are very low which results from lower acceleration electric field, curvature radiation and synchrotron radiation have little contributions to the LW1 and TW2 phase band spectra. The TeV emission of ICS from pairs can be also found for P1, bridge and P2 in our calculated phase-resolved spectra, which are consistent with the modeled TeV light curve. Two types of pairs, CR-induced and ICS-induced, could be therefore confirmed by the spectra of the Crab pulsar, these may be also the origin of the two types of wind pairs in Crab Nebula.

4. CONCLUSIONS AND DISCUSSIONS

Owing to its strong multi-wavelength emission, the famous Crab pulsar is a crucial astrophysical object to distinguish the emission mechanisms from different magnetospheric models. In this paper, we calculated radio, X-ray, γ-ray and TeV light curves, phase-averaged spectrum and phase-resolved spectra in the framework of the 3D annular gap and core gap model with reasonable emission-geometry parameters ($\alpha = 45^{\circ}$ and $\zeta = 63^{\circ}$). It is found that the electric field in the annular gap is huge ($\sim 10^{16}$ eV) in the several tens of neutron star radii and vanishes near the region of $R_{\rm LC}$. The primary particles are accelerated to ultra-relativistic energies, and produce numerous secondary particles (CR and ICS pairs) in the inner region of the annular gap via $\gamma{-}$B process. The pulsed emission of radio, X-ray and γ-ray are generated from the emission of primary particles or secondary particles (pairs) with different emission mechanisms in the nearly similar region of the annular gap (or core gap) in only one pole, this leads to the "phase-aligned" multi-wavelength light curves. The emission of P1 and P2 is originated from the annular gap region near the null charge surface, while the emission of bridge is mainly originated from the core gap region.

Assuming that power-law energy distributions of primary particles and two types of pairs, the phase-averaged spectrum and phase-resolved spectra of the Crab pulsar are well produced by mainly four components: synchrotron radiation from CR-induced and ICS-induced pairs dominates the X-ray band to soft γ-ray band (100 eV to 10 MeV); curvature radiation and synchrotron radiation from the primary particles mainly contribute to γ-ray band (10 MeV to $\sim 20\,$GeV); ICS from the pairs significantly contributes to the TeV γ-ray band (100 GeV to 400 GeV). Our fitted phase-averaged spectrum and phase-resolved spectra have similar tendency varying with the photon energy and are basically consistent with outer gap model (Tang et al. 2008) and the slot gap model (Harding et al. 2008) at soft X-ray to a few tens of GeV band, but quite different in $> 20\,$GeV band. This is mainly due to the additional spectral component of ICS from pairs. From the multi-wavelength spectral fitting we emphasize that curvature radiation alone emitted from the primary particles cannot explain the TeV band (25 to 400 GeV) emission of the phase-averaged spectrum, ICS from pairs significantly contribute to this $> 20\,$GeV band. In addition, two types of pairs are generated in the magnetosphere, and they may be also the origin of the two types of wind pairs in Crab Nebula (Abdo et al. 2010).

Radio emission (1.4 GHz) of the Crab pulsar is originated from a narrow and high-altitude region with a similar location of the γ-ray emission, which leads to the phase-aligned peaks. Our model for radio photon sky-map is patch-like, however the detailed emission mechanism for radio emission is needed to further studied.

The popular outer gap (except the versions of Romani & Yadigaroglu (1995); Cheng et al. (2000); Romani & Watters (2010)) and slot gap models are two-pole models (Tang et al. 2008; Zhang & Li 2009; Li & Zhang 2010; Harding et al. 2008). To model the observed light curves and spectra for the Crab pulsar, they require the emission from the both magnetic poles, which result from larger magnetic inclination angle α or larger viewing angle ζ. However, our annular gap model is an intermediate emission-altitude and single-pole model with reasonable α and ζ from the X-ray torus fitting (Ng & Romani 2008). Unfortunately, the important parameters α and ζ for pulsar emission geometry are uncertain so far. Ng & Romani (2008) can only give a reliable viewing angle ζ for some young pulsars which have X-ray torus configurations, and then combine with the radio rotating vector model (RVM) to obtain the inclination angle α using the radio polarization angle (PA) fitting. The simple RVM model is only based on the geometry at a certain low altitude for an assumed circular emission beam, and the propagation effects that can change the polarization states that had been already ignored by the RVM model. The derived α by this method is therefore debatable. A better method is strongly desired to obtain the convincing values of α and ζ.

To well explain the multi-wavelength pulsed emission from pulsars, the detailed magnetic field configuration and 3D global acceleration electric field distribution with proper boundary conditions for the annular gap and the core gap should be carefully studied. Unfortunately, these two physical aspects are not fully understood. Recnetly, Romani & Watters (2010) studied pulsar light curves with magnetosphere beaming models and found that outer gap model and approximating force-free dipole field were preferred at their high statistical significance. However, Harding et al. (2011) also studied high-energy pulse profiles (e.g. the Vela pulsar) using both retarded vacuum dipole and force-free field geometry. They found that slot gap model with vacuum dipole was more favorable. Therefore, the subject of pulsar magnetic field configuration is still debatable. In addition, the problem of 3D acceleration field with the general relativistic effect and pair screening effect is more complicated, although many efforts have been paid. We just derived the 1D (actually 2D) continuous solution for the acceleration Possion equation, and the general relativistic and pair screening effects have not been taken into account in our annular gap model at present. This is our first step to establish our model picture, and will benefit further 3D complicated physical studies with considerations of related effects. We emphasize that some simplified hypothesis considering qualitative physical effects have been used in our model to study pulsar light curves and spectra. This can give us insightful enlightenments to improve our knowledge of pulsar radiation physics. We will further improve our model to give more precise modeled light curves, especially for the phases of LW1 and TW2.

In sum, the multi-wavelength emission from the Crab pulsar can be well explained in the annular gap and core gap model, and this is also done for the Vela pulsar (Du et al. 2011). Our model is a promising model to unveil the multi-wavelength pulsed emission from γ-ray pulsars.

The authors are very grateful to the referee for the insightful and constructive comments. We thank both the pulsar groups of NAOC and of Peking University for useful conversations. The authors are supported by NSFC (10821061, 10573002, 10778611, 10773016, 11073030 and 10833003) and the Key Grant Project of Chinese Ministry of Education (305001).

Facilities: Fermi (LAT), MAGIC, VERITAS

REFERENCES

Abdo, A. A., et al. 2010, ApJ, 708, 1254
Aleksić, J., Alvarez, E. A., Antonelli, L. A., et al. 2011, ApJ, 742, 43
Blumenthal, G. R., & Gould, R. J. 1970, Reviews of Modern Physics, 42, 237
Cheng, K. S., Ho, C., & Ruderman, M. 1986a, ApJ, 300, 500
Cheng, K. S., Ho, C., & Ruderman, M. 1986b, ApJ, 300, 522
Cheng, K. S., Ruderman, M., & Zhang, L. 2000, ApJ, 537, 964
Daugherty, J. K., & Harding, A. K. 1994, ApJ, 429, 325
Daugherty, J. K., & Harding, A. K. 1996, ApJ, 458, 278
Du, Y. J., Xu, R. X., Qiao, G. J., & Han, J. L. 2009, MNRAS, 399, 1587
Du, Y. J., Qiao, G. J., Han, J. L., Lee, K. J., Xu, R. X. 2010, MNRAS, 406, 2671
Du, Y. J., Han, J. L., Qiao, G. J., & Chou, C. K. 2011, ApJ, 731, 2
Dyks, J., & Rudak, B. 2003, ApJ, 598, 1201
Erber, T. 1966, Reviews of Modern Physics, 38, 626
Fang, J., & Zhang, L. 2010, ApJ, 709, 605
Goldreich, P., & Julian, W. H. 1969, ApJ, 157, 869
Harding, A. K., Stern, J. V., Dyks, J., & Frackowiak, M. 2008, ApJ, 680, 1378
Harding, A. K., DeCesar, M. E., Miller, M. C., Kalapotharakos, C., & Contopoulos, I. 2011, arXiv:1111.0828
Hirotani, K. 2008, ApJ, 688, L25
Hobbs, G. B., Edwards, R. T., & Manchester, R. N. 2006, MNRAS, 369, 655
Kuiper, L., Hermsen, W., Cusumano, G., Diehl, R., Schönfelder, V., Strong, A., Bennett, K., & McConnell, M. L. 2001, A&A, 378, 918
Lee, K. J., Du, Y. J., Wang, H. G., Qiao, G. J., Xu, R. X., & Han, J. L. 2010, MNRAS, 405, 2103
Li, X., & Zhang, L. 2010, ApJ, 725, 2225
Lin, G. F., & Zhang, L. 2009, ApJ, 699, 1711
MAGIC Collaboration, Aleksić, J., Alvarez, E. A., et al. 2011, arXiv:1109.6124
Manchester, R. N., Hobbs, G. B., Teoh, A., & Hobbs, M. 2005, AJ, 129, 1993
Meng, Y., Zhang, L., & Jiang, Z. J. 2008, ApJ, 688, 1250
Muslimov, A. G., & Harding, A. K. 2003, ApJ, 588, 430
Muslimov, A. G., & Harding, A. K. 2004, ApJ, 606, 1143
Ng, C.-Y., & Romani, R. W. 2008, ApJ, 673, 411
Qiao, G. J., & Lin, W. P. 1998, A&A, 333, 172
Qiao, G. J., Lee, K. J., Wang, H. G., Xu, R. X., & Han, J. L. 2004a, ApJL, 606, L49
Qiao, G. J., Lee, K. J., Zhang, B., Xu, R. X., & Wang, H. G. 2004b, ApJL, 616, L127
Qiao, G. J., Lee, K. J., Zhang, B., Wang, H. G., & Xu, R. X. 2007, Chinese Journal of Astronomy and Astrophysics, 7, 496
Romani, R. W., & Yadigaroglu, I.-A. 1995, ApJ, 438, 314
Romani, R. W., & Watters, K. P. 2010, ApJ, 714, 810
Ruderman, M. A., & Sutherland, P. G. 1975, ApJ, 196, 51
Tang, A. P. S., Takata, J., Jia, J. J., & Cheng, K. S. 2008, ApJ, 676, 562
VERITAS Collaboration, Aliu, E., Arlen, T., et al. 2011, Science, 334, 69
Zhang, B., Qiao, G. J., Lin, W. P., & Han, J. L. 1997a, ApJ, 478, 313
Zhang, B., Qiao, G. J., & Han, J. L. 1997b, ApJ, 491, 891
Zhang, L., & Cheng, K. S. 1997, ApJ, 487, 370
Zhang, L., Cheng, K. S., Jiang, Z. J., & Leung, P. 2004, ApJ, 604, 317
Zhang, L., Fang, J., & Chen, S. B. 2007, ApJ, 666, 1165
Zhang, L., & Li, X. 2009, ApJ, 707, L169